A NEW MICRO-HYDRODYNAMIC HERRINGBONE BEARING USING SLANT GROOVE DEPTH ARRANGEMENTS FOR PERFORMANCE ENHANCEMENT

Y. T. Lee A. S. Yang Y. H. Juan

Department of Energy and Refrigerating Air-Conditioning Engineering
National Taipei University of Technology
Taipei, Taiwan

C. S. Liu* Y. H. Chang

Department of Mechanical Engineering and Advanced Institute of Manufacturing with High-Tech Innovations
National Chung Cheng University
Chiayi, Taiwan

ABSTRACT

This study presents a new groove profile using the slant groove depth arrangements to enhance the performance of micro-HGJBs. The computational analysis was based on the steady-state three-dimensional conservation equations of mass and momentum in conjunction with the cavitation model to examine the complex lubricated flow field. The simulated results of load capacity and circumferential pressure distribution of lubricant film are in good agreement with the measurement data and the predictions cited in the literature. Numerical experiments were extended to determine the pressure distribution, load capacity, radial stiffness and friction torque by varying the slant ratio of groove depth, eccentricity ratio, rotational speed and attitude angle. The cavitation extent of lubricant film was also studied for different slant groove patterns.

Keywords: Hydrodynamic bearing, Load capacity, Film pressure, CFD.

1. INTRODUCTION

Hydrodynamic bearings have the advantages of low friction, shock resistance and low noise when serving as essential components in rotating machines [1]. Generally, the grooved surfaces are designed to operate with some lubrication since the film formed by the lubricant decreases friction and wear at the contact between two surfaces in a relative sliding motion [2]. Furthermore, the hydrodynamic lubrication is an effective way of preventing leakage and providing load-carrying capacity [3]. In recent times, the well-known herringbone-grooved journal bearings (HGJBs) have been widely developed for modern industrial applications [4].

Herringbone grooves on journal bearings produce lubricants to be pumped inward for reducing side leakage of oil as well as enhancing stiffness and stability of rotational parts, as compared to plain journal bearings. Theoretical and experimental studies have been carried out to explore the design aspects and performance characteristics of hydrodynamic bearings in different kinds of mechanical systems. Zhang *et al*. [5] examined the relationship between the load carrying capacity and misalignment angle for bearings at different relative clearances and length-to-diameter ratios for water-lubricated plain journal bearings. Hirs [6] compared the theoretical predictions with the experimental results and analyzed the load capacity and stability characteristics for grooved bearings. It was found that grooved journal bearings can operate stably at centric and near-center conditions, while plain journal bearings are not stable for that case. Besanjideh *et al*. [7] explored the hydrodynamic behavior of finite length journal bearings under the conditions of laminar flows with variable densities. The results indicated that the load carrying capacity of journal bearing was affected by lubricant compressibility. Scheichl *et al*. [8] developed a new formulation of the cavitation phenomenon occurring in porous journal bearings to gain insight into the development of the lubrication pressure and saturation tied in with the phase changes taking place inside the lubrication gap under fully hydrodynamic lubrication. Kinouchi and Tanaka

* Corresponding author (imecsl@ccu.edu.tw)

DOI : 10.1017/jmech.2017.72
Copyright © 2017 The Society of Theoretical and Applied Mechanics
https://doi.org/10.1017/jmech.2017.72 Published online by Cambridge University Press

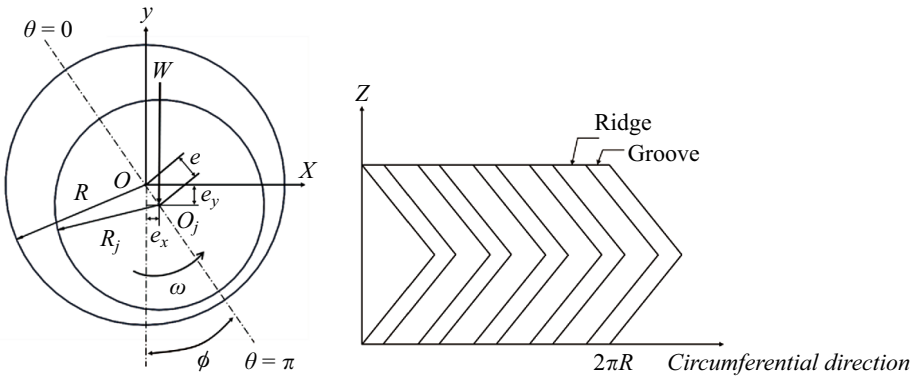
[9] analyzed the performance characteristics of HGJBs having the design of rectangular grooves. Adatepe *et al*. [10] experimentally and numerically investigated tribological performances to determine the friction force, friction coefficient, shaft center orbit and film thickness of non-grooved and micro-grooved journal bearings under dynamic loading. Lee *et al*. [11] proposed a theoretical model to develop a computer simulation program for investigating the effects of different design parameters on the performance of bearing loads for a twin screw air compressor. Chen *et al*. [12] employed the Taguchi parameter design methodology to determine a suitable groove width ratio of 0.4 and a depth ratio of 1.25 for improving load capacity and stability for multi-step reversible rotating HGJBs, as compared to those normal bearings. Chang *et al*. [13] experimentally studied the stability of a herringbone-microgrooved journal bearing in an impeller-spindle system under static radial forces. The test results revealed that the proposed spindle was stable when the Sommerfeld number was less than 59, indicating that the spindle should not operate under an eccentricity ratio of 0.18. Subsequently, Jang and Chang [14] analyzed a HGJB of a spindle motor in a hard disc drive with consideration of the cavitation effect and found that load capacity and bearing torque raised with increasing the eccentricity and length/diameter (L/D) as well as decreasing groove the width ratio. Jang and Yoon [15, 16] explored the dynamic behaviors of a HGJB with plain sleeve and a plain journal bearing with grooved sleeve under static and dynamic load conditions. The escalation of instability of the bearing with rotating herringbone grooves was also noted with increasing eccentricity ratio and with decreasing groove number. Narendiranath Babu *et al*. [17] analyzed the relative strengths and weaknesses of bearings and documented the development in improving bearing measurements. Particularly, vibration and condition monitoring techniques were presented. Yen and Chen [18] utilized novel elliptical grooves to enhance the characteristics of journal bearings. Those optimum groove parameters were identified to be the groove width ratio of 0.5, groove depth ratio of 2.0, and elliptical axis ratio of 1.5 for attaining the maximum radial force. Chen *et al*. [19] ran the stability analysis of a hydrodynamic journal micro-bearing with the design parameters optimized at a groove width ratio of 0.5, a groove angle of 40°, and a groove depth ratio of 1.0 for the condition of bearing length/diameter = 1 to augment the load capacity and stability performance of a HGJB.

It is essential to fully understand the lubricant film flow details before devising various products for practical applications. To predict such difficult flow problems, the computational fluid dynamics (CFD) computer software can be useful as a simulation tool to optimize the design parameters with a substantial reduction in development and testing time. In the past, most computational models for bearing performance evaluation used the Reynolds equation to describe the fluid behavior of the lubricant film under the assumption of the small flow channel. Though the streamwise momentum equation for inertia-free flow induces the basis for the Reynolds equation, its predictions can be relatively less accurate for the problems in which the cross-film pressure gradient may be substantial with the occurrence of consequent secondary flows. Besides, earlier numerical and experimental studies have presented that the geometric design of groove profiles in terms of dimensions and shapes can greatly affect the performance of HGJBs. However, very limited researches were completed to investigate the influence of groove depth on the bearing load characteristics. This research proposed a new groove profile using slant groove depth arrangements to improve the performance of micro- hydrodynamic herringbone grooved bearings. To simulate the inherently complex lubricating flow field, the commercial CFD software ANSYS/Fluent® [20] was employed to conduct the numerical analysis by solving the steady three-dimensional conservation equations of mass and momentum. To validate the present computational model, the predicted load capacity was compared with the measured data of Hirs [6] and the simulated results from Jang and Chang [14] as well as Lee *et al*. [21] at different eccentric ratios for a micro-hydrodynamic bearing. Numerical experiments were extended to evaluate the bearing performance factors including the pressure distribution, load capacity, radial stiffness and friction torque by varying the slant ratio of groove depth, eccentricity ratio, rotational speed and attitude angle for realization of design improvement under hydrodynamic lubrication. The vapor volume fraction distribution was also characterized to investigate the slant groove depth effect on the cavitated region of lubricant film.

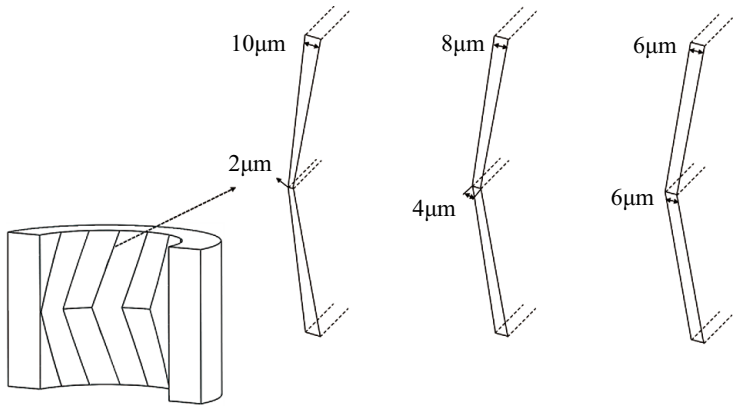
2. DESCRIPTION OF BEARING MODEL

Figure 1 displays the schematics of (a) journal-bearing geometric details in an end view and (b) herringbone grooves in a side view. As an important factor for design considerations, c represents the radial clearance, which is the difference between the bearing and journal radii. The signs O_j, O_b, R_j and R mean the centers and radii of journal and bearing, respectively. In practice, the journal rotates at an angular velocity ω in an equilibrium position under known conditions of stable eccentricity and pressure of the lubricant film. The pressure produced primarily lies in the convergent part of the journal-bearing gap to counteract the external load thereby separating the journal surface from the bearing surface through a thin lubricant film. The hydrodynamic pressure eventually terminates in the divergent part of the gap, where the pressure may drop below the ambient pressure of lubricant. When steady state is attained, the journal is shifted from the bearing with a center distance (e), which is referred to the journal eccentricity. The eccentricity ratio (ε), defined as e/c, and the radial clearance (c) are crucial measures of the load capacity of bearings, whereas the angle between the load direction and the eccentricity orientation is the attitude angle (ϕ). Table 1 illustrates the geometric details of the herringbone grooved bearing. Considering as one of the most extensively used design configuration of

https://doi.org/10.1017/jmech.2017.72 Published online by Cambridge University Press



(a)



(b)

Fig. 1 Schematics of (a) journal-bearing geometric details in an end view and herringbone grooves in a side view; (b) different groove profiles with proposed slant depth designs of 10 to 2, 8 to 4 μm and conventional constant depth design of 6 μm in an enlarged view.

Table 1 Geometric details of herringbone grooved bearing

Parameter	Value
Bearing diameter, D	4 mm
Bearing length, L	4 mm
Bearing width, w	0.78 mm
Radial clearance, c	6 μm
Number of grooves	8
Groove angle, α	70 deg.
Slant groove depth	10 to 2 μm 8 to 4 μm

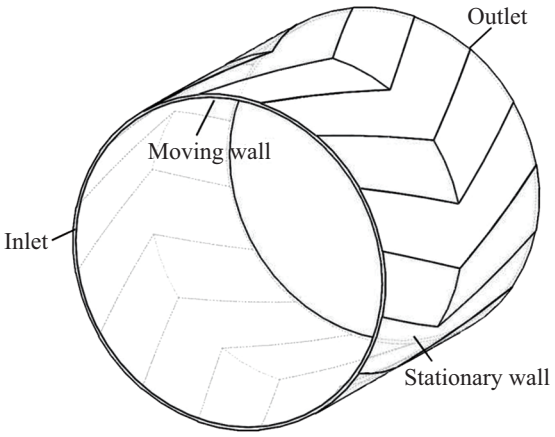


Fig. 2 Computational domain with boundary conditions.

HGJBs [14], the bearing dimensions were 4-mm length, 4-mm diameter and 6-μm clearance, displaying the features of a micro-hydrodynamic bearing in this study. The total number of 70-degree grooves was 8 with the width and depth of 0.78 mm and 6 μm, respectively.

The groove profiles of HGJBs have extensively used the rectangular groove shape with an even depth. The usual way to enhance the loading capacity is reducing the lubricant film thickness; however, this may possibly cause the occurrence of cavitation. This study proposes the new design using a slant groove depth profile as a promising solution. Figure 2 illustrates the schematics of different groove profiles with the proposed slant depth designs of 10 to 2, 8 to 4 μm and the conventional con-

https://doi.org/10.1017/jmech.2017.72 Published online by Cambridge University Press

stant depth design of 6 μm in an enlarged view. The slant depth design shapes a continuous decrease of the lubricant film thickness from the divergent side to the convergent side of grooves, which could boost the lubricant film flowing toward the center area and enhance load capacity of HGJBs. In this study, the average groove depth is maintained at 6 μm, whereas the depths of grooves for the slant depth design decrease from 10 to 2 and 8 to 4 μm, respectively, for ensuring the same basis of fair comparison with a conventional bearing having a 6-μm constant depth.

3. THEORETICAL FORMULATION

A theoretical formulation built in the ANSYS/Fluent® software release 16 was utilized to simulate the flow phenomena for grooved micro-hydrodynamic bearings. In this study, a rigid bearing was assumed because the lubricant film thickness is substantially less than the bearing radius with an external load applied to the journal. The bearing models were specifically created from their dimensions and curvature details. The solid models were then readily transferred to the preprocessor of the CFD software ANSYS/Fluent® for constructing the numerical models, utilizing the grids generator module ANSYS Meshing®. Calculations were performed via the ANSYS/Fluent® software to resolve the velocity and pressure fields for investigating the loading characteristics of grooved bearings. Considering the flows involving compressibility dynamics of the cavitating bubble-liquid mixture with an insignificant gravity effect, the analysis was based on the steady three-dimensional (3D) conservation equations of mass and momentum in conjunction with the cavitation model to examine the lubricated flow process for evaluation of the bearing performance under stable operations. The corresponding Reynolds numbers of flows range from 9.25 to 46.27 (for the diameter of 4 mm and rotational speed from 1500 to 7500 rpm), suggesting laminar flows in nature. The governing equations are given as below:

$$\frac{\partial \rho u_k}{\partial x_k} = 0. \tag{1}$$

$$\frac{\partial(\rho u_i u_j)}{\partial x_j} = -\frac{\partial p}{\partial x_i} + \frac{\partial}{\partial x_j}\left[\mu\left(\frac{\partial u_i}{\partial x_j} + \frac{\partial u_j}{\partial x_i}\right) - \frac{\partial}{\partial x_i}\left[\frac{2}{3}\mu\left(\frac{\partial u_k}{\partial x_k}\right)\right]\right]. \tag{2}$$

The variable u_i indicates the velocity component in the i direction; moreover, p, ρ and μ are the pressure, density and dynamic viscosity of lubricant oil. In operations, the lubricating film pressure may drop under its saturation vapor pressure, leading to a rupture of the liquid with formation of cavitation, which needs to be treated to correctly handle the pressure in the divergent part of a bearing at high eccentricities. In such a process, very large and steep density variations occur in the cavitating regions. The vapor transport equation in ANSYS/Fluent® is used to simulate the liquid–vapor mass transfer (vaporization and condensation) [22, 23].

$$\frac{\partial(\alpha_v \rho_v)}{\partial t} + \frac{\partial}{\partial x_i}(\alpha_v \rho_v u_{vi}) = R_e - R_c \tag{3}$$

Here α_v, ρ_v and u_{vi} signify the volume fraction, density and velocity component in the i axis for the vapor phase. The symbols R_e and R_c represent the mass transfer source terms related to vapor generation (evaporation) and condensation rates, elucidating the mass transfer between the liquid and vapor phases in the cavitation process. In a flowing liquid with zero velocity slip between the fluid and bubbles, the Rayleigh-Plesset equation is utilized to model the bubble dynamics of growth and collapse of vapor bubbles as below.

$$R_b \frac{d^2 R_b}{dt^2} + \frac{3}{2}\left(\frac{dR_b}{dt}\right)^2 = \left(\frac{p_b - p}{\rho}\right) - \frac{2\sigma}{\rho R_b} - 4\frac{\mu}{\rho R_b}\frac{dR_b}{dt}, \tag{4}$$

where R_b, p_b, p and σ denote the bubble radius, bubble surface pressure, exterior pressure far from the bubble and bubble surface tension, respectively. Neglecting the second-order terms and the surface tension force, Eq. (4) can be simplified to

$$\frac{dR_b}{dt} = \sqrt{\frac{2}{3}\frac{p_b - p}{\rho}}, \tag{5}$$

From Eq. (5), the bubble dynamics effects are incorporated into the cavitation model to take void propagation into account. In this study, Zwart-Gerber-Belamri model was used assuming no interactions among all the bubbles (i.e. low vapor volume fraction) in a system to compute the interphase mass transfer rate. The final form of the cavitation model is given as below.

$$\text{If } p \le p_v; \quad R_e = F_{evap}\frac{3\alpha_{nuc}(1-\alpha_v)\rho}{R_b}\sqrt{\frac{2}{3}\frac{p_v - p}{\rho}}, \tag{6}$$

$$\text{If } p \ge p_v; \quad R_c = F_{cond}\frac{3\alpha_v \rho_v}{R_b}\sqrt{\frac{2}{3}\frac{p - p_v}{\rho}}. \tag{7}$$

The values of the bubble radius (R_b), volume fraction of the nucleation site (α_{nuc}), evaporation coefficient (F_{evap}) and condensation coefficient (F_{cond}) were prescribed as 10^{-6} m, 5×10^{-4}, 50 and 0.01, respectively.

As the pressure distribution of the lubricant film is solved, the radial and tangential loads (i.e. the forces acting along and normal to the line of center, respectively) can be determined by integrating the pressure over the journal surface as below.

$$F_R = -\iint_S p\cos\varphi dxdz, \quad F_T = \iint_S p\sin\varphi dxdz \tag{8}$$

The load carrying capacity W can be calculated by

$$W = \sqrt{F_R^2 + F_T^2}. \tag{9}$$

Based on the coordinate system given in Fig. 1, the attitude angle ϕ is determined as below [24].

$$\phi = 90 - \tan^{-1}(e_x/(-e_y)). \tag{10}$$

https://doi.org/10.1017/jmech.2017.72 Published online by Cambridge University Press

The friction torque of a bearing can be determined from the integration of the shear stress τ_{yx} along the lubricant film.

$$T = R\iint_S \tau_{yx} dxdy. \quad (11)$$

To consider the scenarios during operations, the range of the eccentricity ratio of the bearing was from 0.1 to 0.7, with the rotating speed and attitude angle varied from 1500 to 7500 rpm and 0 to 90°, respectively. Because this study mainly investigates the bearing performance improvement using the new slant groove design; hence, the proposed bearing was considered to be immersed in a constant temperature oil bath environment at 20°C to neglect the thermal effect for simplification of the problem. Utilizing SAE30 lubricating oil as the working fluid, the density and viscosity of lubricant were 881.5 kg/m^3 and 0.23939 N-s/m^2 at the operating temperature of 20°C as the baseline case for the bearing performance analysis [25]. Besides, to characterize the cavitating process, the saturation vapor pressure of the lubricant was 1 Pa, whereas the saturation density and dynamic viscosity of the lubricant vapor were 10.95 kg/m^3 and 7×10^{-6} N-s/m^2, respectively [26].

Figure 2 exhibits the computational domain with the associated boundary conditions. To perform CFD simulations, one side of the lubricant film clearance is used as an inlet and the other as an outlet to simplify the geometry, whereas the boundary conditions at the inlet and outlet were set as the modes of pressure inlet and pressure outlet at 1 atm. The gap between the journal and bearing was filled with lubricant. The outer and inner surfaces of the lubricant film were modeled as a stationary wall and a moving wall at various rotational speeds of the journal. The no-slip boundary condition was imposed on the bearing and shaft surfaces. The zero normal gradient of pressure was imposed on the solid wall adjacent to the lubricant film. The governing equations were discretized by the finite control volume approach to replace the partial differential equations with algebraic equations. Using the staggered-grid setup, the grids of velocities were segregated from grids of scalars and laid directly on the surfaces of the control volumes for estimating the convective fluxes across cell surfaces. An iterative semi-implicit method for pressure-linked equations consistent (SIMPLEC) algorithm was utilized for the velocity- pressure coupling [27, 28]. The under-relaxation technique was also implemented to circumvent divergence during iterations. For each steady-state calculation, the normalized residual errors of flow variables were required to converge to 10^{-6} with mass balance check less than 0.5%. Overall, each solution procedure was found to take roughly 10 hours of the central processing unit time (CPU) when executed on an Intel® Xeon® E5-2670 v3-2.3 GHz (× 2 processors, 192 GB RAM) high-performance workstation to achieve a converged solution.

4. RESULTS AND DISCUSSION

Numerical calculations were conducted by the CFD code ANSYS/Fluent® to validate the present computational model by comparing the predictions with the experimental results from the literature. The numerical models were built and meshed in ANSYS Workbench® 16. More grid points were added to place on the original geometrical shape for local grid refinement. In practice, the unstructured prism meshes were generated for the boundary layer near the walls with the mixed mesh of tetrahedral and hexa for fitting to the geometry and boundaries of the bearing. The values of the minimum orthogonal quality, maximum aspect ratio and maximum cell skewness were 0.71, 4.43 and 0.83, respectively, suggesting realization of a reasonably good quality mesh.

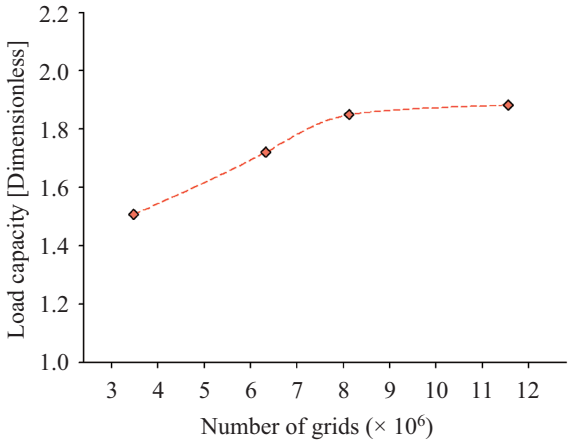


Fig. 3 Predicted dimensionless load capacities at different grids for grid independence test.

Figure 3 illustrates the predicted dimensionless load capacities estimated using different grids at an eccentricity ratio of 0.4 and 5000 rpm for the grid independence test. As the total number of grids increases from 3476253 to 11551684, it was observed that the load capacity approaches an even state asymptotically. The discrepancy of load capacity was 25.3% with the 3476253 grids and the 11551684 grids. The difference of computed load capacity was still 10.1% with the 6724758 grids and the 11551684 grids. However, the corresponding variation of the predictions reduced to 1.9% for the mesh systems based on the 8124932 and 11551684 grids. It is suggested that a mesh setup of 8124932 grids can be used to attain satisfactory grid independence for ensuring that the predictions of load carrying capacity are not affected by different meshes.

To validate the present computational model, two simulation cases were carried out with the calculated results compared against the experimental data [6, 29] and the predictions [14, 21], respectively. The details of geometrical extent and operational conditions for those two cases are given in Ref. 21. The first case considered a plain journal bearing with no grooves on the surfaces of the shaft and bush, whereas the second case studied a typical HGJB model from Hirs [6] and Jang and Chang [14]. Figure 4 presents a comparison of (a) the computed dimensionless pressure ($\frac{P}{\mu\omega}\left(\frac{c}{R}\right)^2$)

https://doi.org/10.1017/jmech.2017.72 Published online by Cambridge University Press

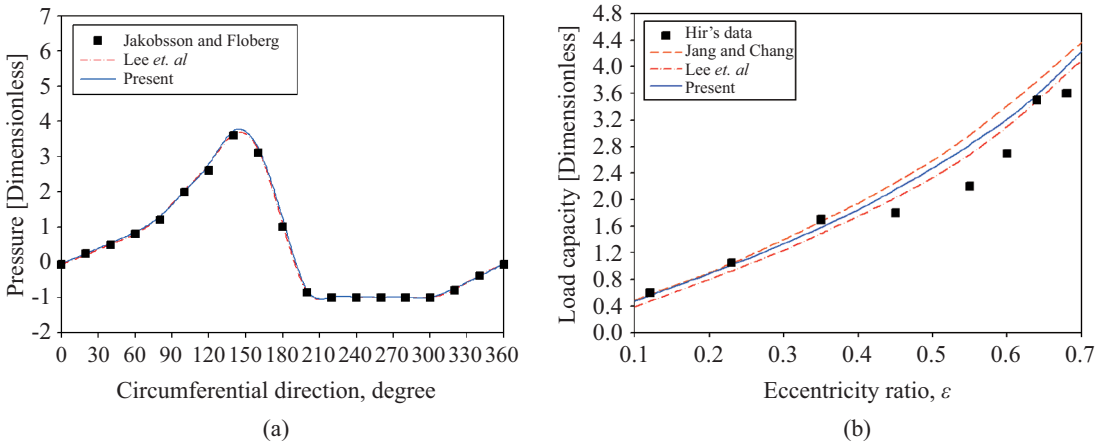


Fig. 4 Comparison of (a) calculated dimensionless circumferential pressure distribution with experimental data [28] and predictions [21] as well as (b) calculated dimensionless load capacities at different eccentricity ratios with measurements [6] and predictions [14, 21].

Table 2 Test Matrix for Simulation Conditions

Case	Eccentricity Ratio	Rotational Speed (rpm)	Attitude Angle (degree)
1	0.1	4500	0
2	0.2	4500	0
3	0.3	4500	0
4*	0.4	4500	0
5	0.5	4500	0
6	0.6	4500	0
7	0.7	4500	0
8	0.4	1500	0
9	0.4	2500	0
10	0.4	3500	0
11*	0.4	4500	0
12	0.4	5500	0
13	0.4	6500	0
14	0.4	7500	0
15*	0.4	4500	0
16	0.4	4500	15
17	0.4	4500	30
18	0.4	4500	45
19	0.4	4500	60
20	0.4	4500	75
21	0.4	4500	90

*Cases corresponding to the baseline condition

distribution along the circumferential direction with the experimental data [28] and the predictions [21] for case 1 as well as (b) the calculated dimensionless load capacities ($\frac{W}{\mu\omega R^2}\left(\frac{c}{R}\right)^2$) at varied eccentricity ratios with the measured [6] and the predictions [14, 21] for case 2. As shown in Fig. 4(a), the circumferential pressure profile continuously rose until reaching its highest point at approximately 150° and descended rapidly below the atmospheric pressure at around 190° for the case of a plan journal bearing. The greatest difference of predicted peak pressure and measurements was 2.1%. In general, the CFD predictions are consistent with the measured data from Jakobsson and Floberg [29] and numerical results by Lee *et al*. [21]. On the other hand, the computed dimensionless load capacity of a HGJB (given in Fig. 4(b)) escalates with increasing eccentricity ratio and agrees reasonably well with the measured [6] and theoretical results [14, 21]. The validation shows that the

https://doi.org/10.1017/jmech.2017.72 Published online by Cambridge University Press

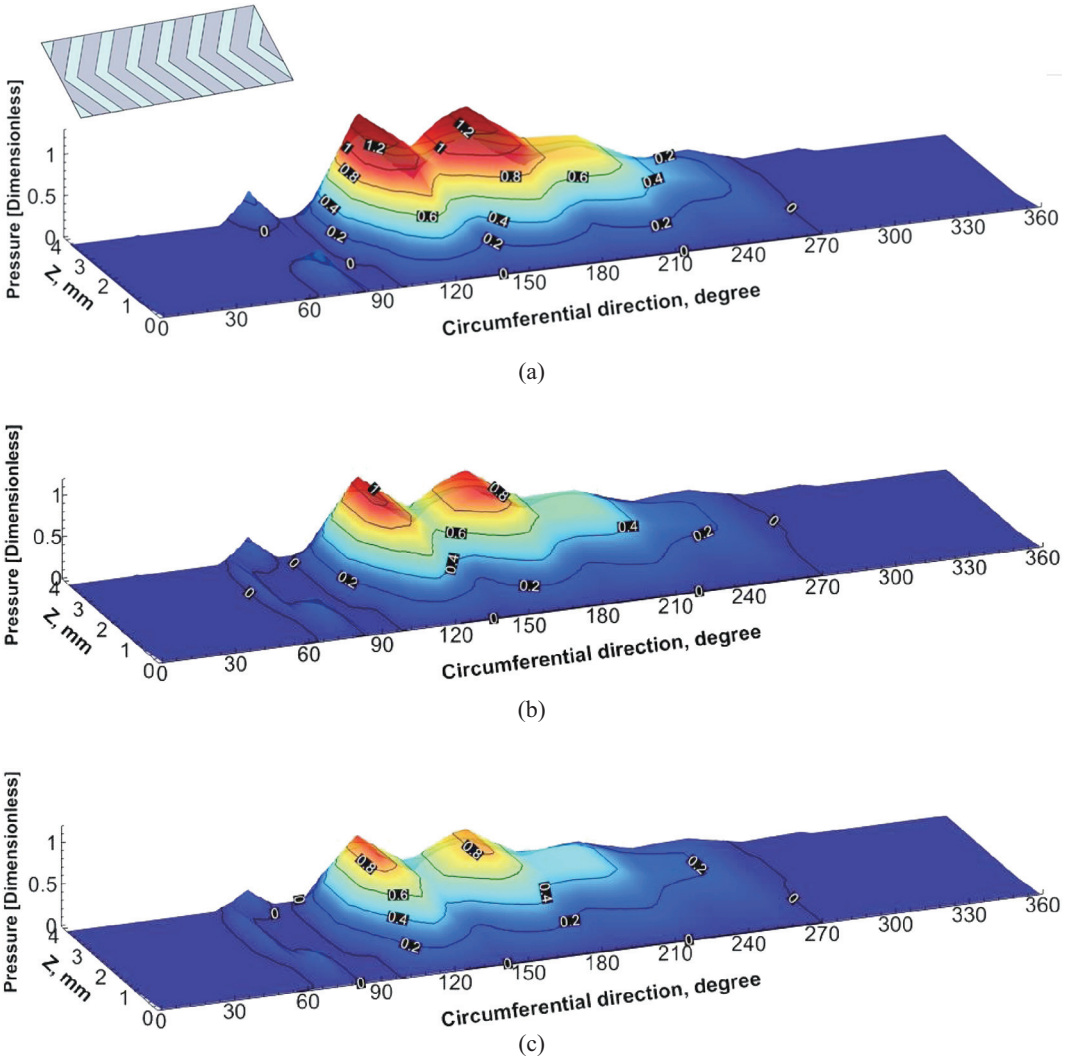


Fig. 5 Predicted dimensionless pressure distributions of lubricant film at an eccentricity ratio of 0.4 and 4500 rpm for micro-hydrodynamic HGJBs with slant depth designs of (a) 10 to 2 μm, (b) 8 to 4 μm and (c) the conventional constant depth design of 6 μm.

present model is reliable and accurate enough to predict the bearing performance. Using the validated bearing model having the extents of 4 mm long, 4 mm diameter (L/D = 1) and 70-degree grooves with the width and depth of 0.78 mm and 6 μm, the following study examined the performance improvement of the proposed new slant groove depth design for a micro-hydrodynamic bearing.

The elucidation of pressure distribution can be helpful to better understand the loading characteristics of HGJBs. Figure 5 exhibits the predicted dimensionless pressure distributions of lubricant film at an eccentricity ratio of 0.4 and 4500 rpm for micro-hydrodynamic HGJBs with the slant depth designs of (a) 10 to 2 μm, (b) 8 to 4 μm and (c) the conventional constant depth design of 6 μm. The bearing angle (θ) was designated corresponding to the maximum and minimum lubricant film thicknesses at θ = 0 and π, respectively. Variations of the pressure profiles were then examined to verify whether the proposed slant depth designs can achieve desired performance. Caused by rotational motion of the shaft, the lubricant flowed toward the center region of the bearings to enhance the pressure loading and diminish the oil leakage. It was visualized that the red streaks indicated those areas at elevated pressures developed by the hydrodynamic lubricant film, whereas the loading performance primarily related to the buildup of positive pressure over the bearing surfaces. In operations, the pressure distribution became nearly wavy shapes in $45° \leqq \theta \leqq 270°$ as a consequence of the presence of grooves over bearing surfaces. In the circumferential axis, the maximum dimensionless pressure of 1.32 for the case of a slant depth groove of 10 to 2 μm was larger than that of 1.06 for the typical model by 24.5%. This can be primarily attributed to the fact that the hydrodynamic lubricating fluid is pressurized by the wedge effect in the slant groove portion. Furthermore, the lubricant film pressure could decline below the ambient pressure to induce the occurrence of cavitation. Essentially, the film pressures for the configurations of slant depth grooves of 10 to 2 μm and 8 to 4 μm were significantly greater than those of 6-μm constant depth grooves, suggesting better hydrodynamic performances of HGJBs attained for those grooves with greater slanted depths.

https://doi.org/10.1017/jmech.2017.72 Published online by Cambridge University Press

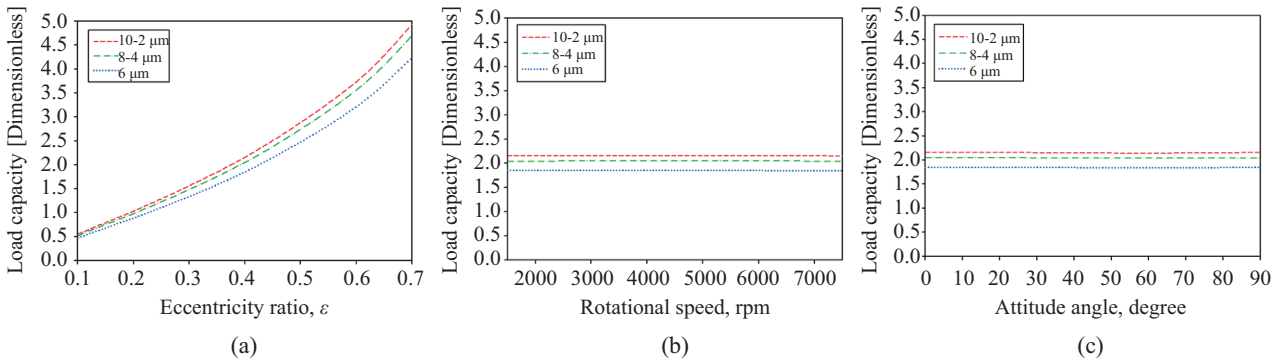


Fig. 6 Predicted dimensionless load capacity with respect to (a) eccentricity ratio (at 4500 rpm and ϕ = 0°), (b) rotational speed (at ε = 0.4 and ϕ = 0°) and (c) attitude angle (at ε = 0.4 and 4500 rpm) for micro-hydrodynamic HGJBs with slant depth designs of 10 to 2, 8 to 4 μm and the conventional constant depth design of 6 μm.

Table 3 Comparison of loading performance of for several HGJBs.

Reference	Hydrodynamic bearing size (diameter, mm × length, mm)	Load capacity [a] [Dimensionless]	Eccentricity ratio	Approach
Gad et al. 2006 [4]	50.4 × 44.5	1.95 - 2.25	0.65 – 0.7	Experiment
Hirs 1965 [6]	N/A [b]	0.60 - 3.6	0.1 – 0.7	Experiment
Kang *et al*. 1966 [13]	N/A	0.40 – 3.6	0.1 – 0.7	Prediction
Chao and Huang 2005 [30]	4.0 × 4.0	0.32 – 3.36	0.1 – 0.7	Prediction
Chen *et al*. 2015 [31]	0.60 × 2.4	0.40 – 3.40	0.1 – 0.7	Prediction
Kawabata *et al*. 1989 [32]	N/A	0.32 – 3.6	0.1 – 0.7	Prediction
Present study [c]	4.0 × 4.0	0.51 - 4.84	0.1 – 0.7	Prediction

[a] Dimensionless formula: $\overline{W} = \dfrac{W}{\mu\omega LD}\left(\dfrac{c}{R}\right)^2$

[b] N/A: not available

[c] Grooves with slant depth of 10-2 μm

For a certain bearing, the load carrying capacity can be closely related to the operating factors including the eccentricity ratio, rotational speed and attitude angle. The formation of adequately high pressures in the lubricant film can provide better load support and maintain stronger integrity of the film. Figure 6 shows the predicted dimensionless load capacity with respect to the (a) eccentricity ratio (at 4500 rpm and ϕ = 0°), (b) rotational speed (at ε = 0.4 and ϕ = 0°) and (c) attitude angle (at ε = 0.4 and 4500 rpm) for micro-hydrodynamic HGJBs with the slant depth designs of 10 to 2, 8 to 4 μm and the conventional constant depth design of 6 μm. In general, the bearings for all three cases revealed a nearly linear increase of the load carrying capacity with respect to the eccentricity ratio. The proposed slant depth design of 10 to 2 μm produced elevated lubricant film pressures, and thereby resulted in 16.8% and 16.3% higher load capacity values of HGJBs than those of the typical design having a 6-μm level depth for load performance enhancement at the eccentricity ratios of 0.7 and 0.4, respectively. Since the increasing tendency of the load capacity (W) was nearly the same as the rotational speed (ω), the variations of dimensionless load carrying capacity (determined by $\dfrac{W}{\mu\omega R^2}\left(\dfrac{c}{R}\right)^2$) were insignificant (Fig. 6(b)) as the rotation rate was increased, indicating the virtually stable loading behavior over a wide range of speed of revolution. The predictions for the new design revealed greater load ratings for bearings than those of the conventional design by 16.7% and 16.3% at 7500 and 4500 rpm. Similarly, the computed results in Fig. 6(c) illustrated that the variations of load capacity were within 2% over the attitude angle range of 0-90°, suggesting that the proposed slant depth grooves can generate the endurable lubricant film pressure for bearing operations in any attitude angle. The prior studies have concentrated on performance improvement of HGJBs. Table 3 illustrates a comparison of the loading characteristics in the associated eccentricity ranges for HGJBs at different sizes. The maximum dimensionless load capacity of 4.84 for the grooves with a slant depth of 10-2 μm was superior to those results from other studies, indicating effectiveness of the slant depth design to enhance the loading performance of hydrodynamic bearings.

https://doi.org/10.1017/jmech.2017.72 Published online by Cambridge University Press

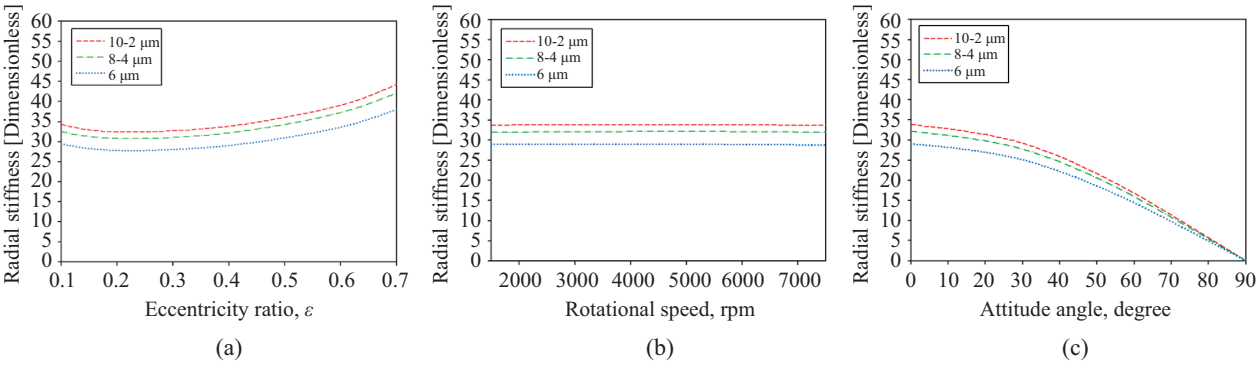


Fig. 7 Predicted dimensionless radial stiffness with respect to (a) eccentricity ratio (at 4500 rpm and $\phi = 0°$), (b) rotational speed (at $\varepsilon = 0.4$ and $\phi = 0°$) and (c) attitude angle (at $\varepsilon = 0.4$ and 4500 rpm) for micro-hydrodynamic HGJBs with slant depth designs of 10 to 2, 8 to 4 μm and the conventional constant depth design of 6 μm.

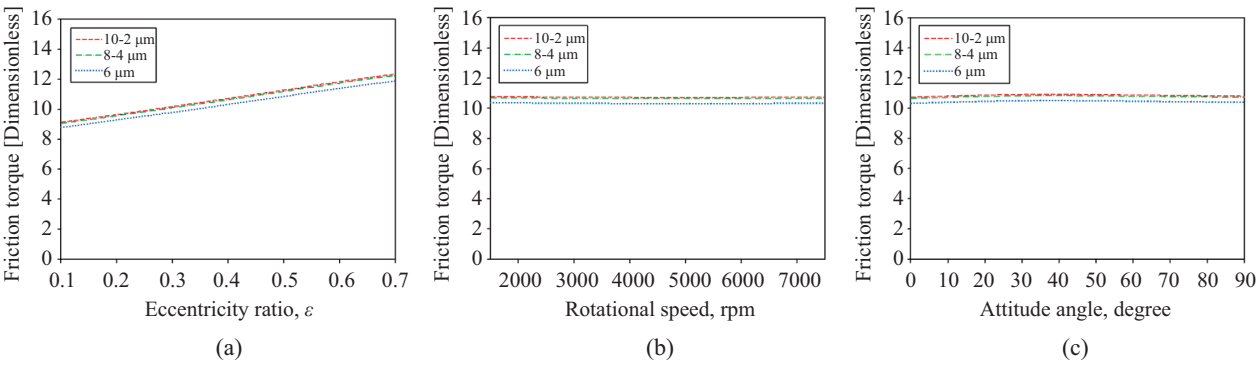


Fig. 8 Predicted dimensionless friction torque with respect to (a) eccentricity ratio (at 4500 rpm and $\phi = 0°$), (b) rotational speed (at $\varepsilon = 0.4$ and $\phi = 0°$) and (c) attitude angle (at $\varepsilon = 0.4$ and 4500 rpm) for micro-hydrodynamic HGJBs with slant depth designs of 10 to 2, 8 to 4 μm and the conventional constant depth design of 6 μm.

The higher film pressure development essentially maximizes radial stiffness to maintain the bearing stability against the radial displacement of the rotor. Figure 7 shows the predicted dimensionless radial stiffness (defined as $\frac{2\pi\overline{W}\cos\phi}{\varepsilon}$) with respect to the (a) eccentricity ratio (at 4500 rpm and $\phi = 0°$), (b) rotational speed (at $\varepsilon = 0.4$ and $\phi = 0°$) and (c) attitude angle (at $\varepsilon = 0.4$ and 4500 rpm) for micro-hydrodynamic HGJBs with the slant depth designs of 10 to 2, 8 to 4 μm and the typical constant depth design of 6 μm. The simulated results from the figure showed that the radial stiffness tended to slightly declined at low eccentricity ratios ($\varepsilon \leqq 0.3$) and grew at $\varepsilon \geqq 0.3$ attributable to substantial increase of the bearing load carrying capacity at high eccentricity values. The calculated radial stiffness values of 44.2 and 42.8 for two new designs were about 16.3% and 12.6% greater than that of a conventional bearing with a level depth of 6 μm at $\varepsilon = 0.7$. Similar to the case of load capacity, the predictions of radial stiffness remained nearly constant with respect to the rotational speed up to 7500 rpm for those three grooves. The radial stiffness of the slant depth design of 10 to 2 μm was around 16.0% higher than that of a conventional model. In addition, it was found that the results of radial stiffness generally lessened due to the factor of $\cos\phi$ in response to increasing attitude angle up to 90°. The calculations of radial stiffness for the slant depth models of 10 to 2 and 8 to 4 μm were greater than that of a customary 6-μm constant depth groove by 16.0% and 12.1% at $\phi = 0°$, respectively.

Bearings with different groove shapes were analyzed using CFD simulations to examine the slant depth design effect on the friction performance of HGJBs journal at varied operating scenarios. Figure 8 illustrates the predicted dimensionless friction torque ($\frac{T}{\mu\omega R^3}\left(\frac{c}{R}\right)$) with respect to the (a) eccentricity ratio (at 4500 rpm and $\phi = 0°$), (b) rotational speed (at $\varepsilon = 0.4$ and $\phi = 0°$) and (c) attitude angle (at $\varepsilon = 0.4$ and 4500 rpm) for micro-hydrodynamic HGJBs with the slant depth designs of 10 to 2, 8 to 4 μm and the conventional constant depth design of 6 μm. For three groove designs, the predicted dimensionless friction torque increased with the eccentricity ratio within the range of 0.1 to 0.7. In fact, the friction torque could be closely related to friction force caused by shear stress of lubricant film. The bearing with the slant depth design of 10 to 2 μm revealed rela-

https://doi.org/10.1017/jmech.2017.72 Published online by Cambridge University Press

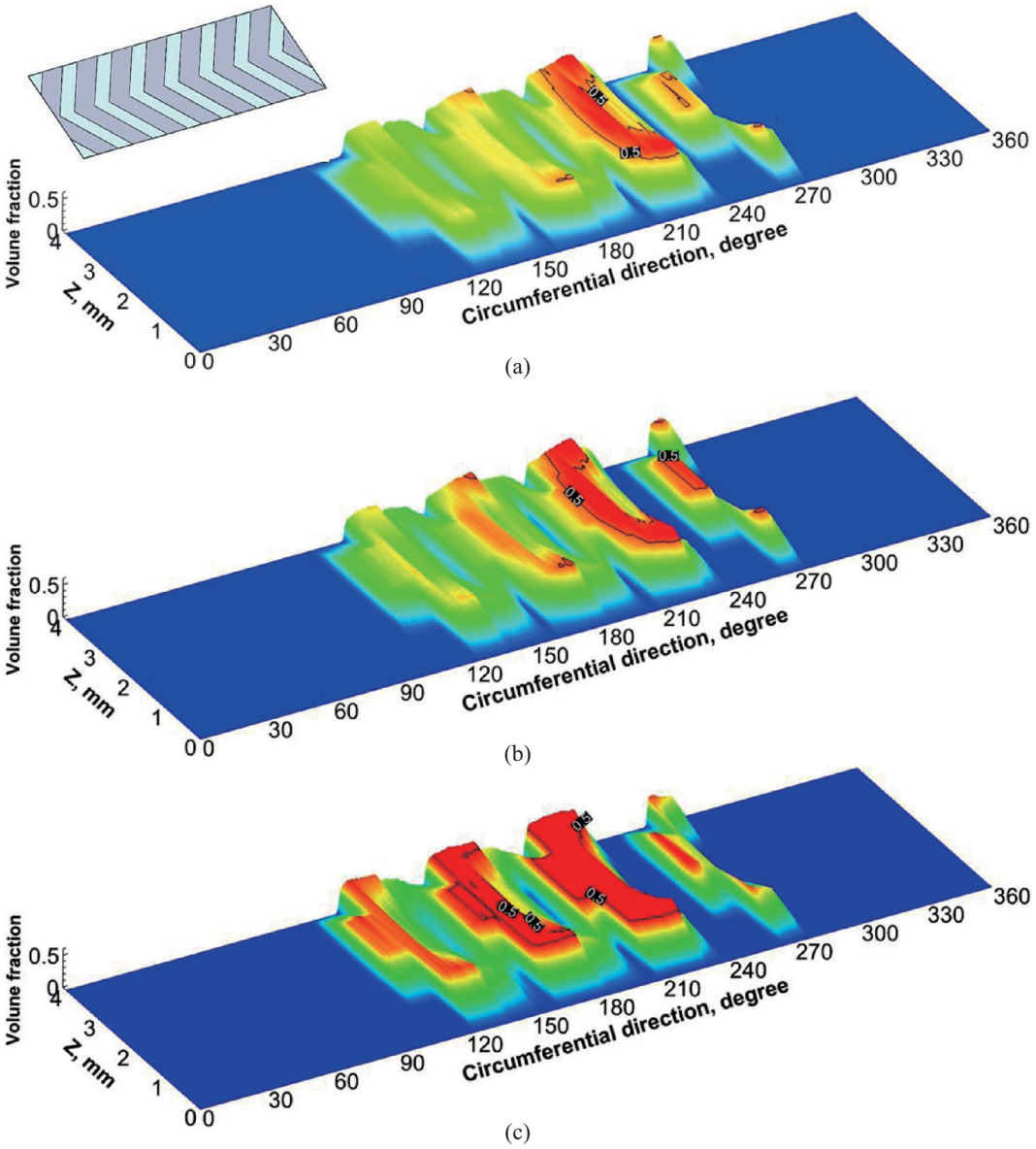


Fig. 9 Predicted vapor volume fraction distributions of lubricant film showing cavitated regions at $\varepsilon = 0.4$, 4500 rpm and $\phi = 0°$ for micro-hydrodynamic HGJBs with slant depth designs of (a) 10 to 2 μm, (b) 8 to 4 μm and (c) the conventional constant depth design of 6 μm.

tively higher velocity gradients and viscous shear stresses as a result of a taper groove, and thereby produced a slightly greater dimensionless friction torque than that for a level groove depth by 3.86% at an eccentricity ratio of 0.4. The predicted dimensionless friction torque revealed nearly uniform with respect to the rotating speed and attitude angle. For the bearings operated at $\varepsilon = 0.4$, the predictions of friction torque of HGJBs with a slant groove depth of 10-2 μm were 3.86% higher than those with a 6-μm level depth for the cases of 4500 rpm (in Fig. 8(b)) or $\phi = 0°$ (in Fig. 8(c)).

During the operations of HGJBs, the occurrence of cavitations could cause a rupture of the lubricant film, and thereby influenced the tribology performance. Figure 9 illustrates the predicted vapor volume fraction distributions of lubricant film showing cavitated regions at $\varepsilon = 0.4$, 4500 rpm and $\phi = 0°$ for micro-hydrodynamic HGJBs with the slant depth designs of (a) 10 to 2 μm, (b) 8 to 4 μm and (c) the conventional constant depth design of 6 μm. To examine the vapor-liquid spreading of lubricant film, the vapor volume fraction contour of 0.5 is used to identify the interfacial location for visualization purpose. It was observed that the highly cavitated regions (marked in a red color) primarily resided in the center with an extension toward two ends of the groove within the bearing angle of 210°- 240° for the case with a slant depth of 10 to 2 μm. An increase in the cavitated regions was found for a relatively less inclined depth of 8 to 4 μm, whereas the largest area of the intense cavitated regions was identified for the model of a 6-μm level depth. To evaluate the cavitation extent, the total vapor volumes of 0.126, 0.137 and 0.165 mm^3 for the grooves of slant depths of 10-2 μm, 8-4 μm and a fixed depth of 6 μm were obtained using an integral of the vapor volume

https://doi.org/10.1017/jmech.2017.72 Published online by Cambridge University Press

fraction with respect to the numerical cell volume over the computational domain of lubricant film. As compared to the bearing having a slant depth of 10-2 μm, the conventional grooved model with a 6-μm even depth revealed an escalation in vapor volume of cavities by around 31%.

5. CONCLUSIONS

This study proposed a new groove profile using the slant groove depth arrangements to improve the performance of micro-hydrodynamic herringbone grooved bearings. The full 3D Navier-Stoke equations of lubricant flow were solved to better understand the pumping effect of HGJBs. To validate the present computational model, the CFD predictions of load carrying capacity and circumferential pressure profile of lubricant film agree reasonably well with the measured data and the simulation results from the literature. Computations were performed to investigate the bearing performance comprising the pressure distribution, radial stiffness, load carrying capacity and friction coefficient under various operating conditions. At the baseline condition of the eccentricity ratio of 0.4, rotating speed of 4500 rpm and attitude angle of 0°, the HGJBs with slant depth grooves of 10 to 2 μm showed relatively greater dimensionless load capacity and radial stiffness than those of typical 6-μm level depth grooves by 16.3% and 16.0%, respectively. Nonetheless, there was discovered a slight increase in friction torque by 3.86% for the new groove design. To evaluate the cavitation extent, the conventional grooved bearing with a 6-μm even depth showed a higher total vapor volume than that of the bearing having a slant depth of 10 to 2 μm by 31%. Simulations have showed the efficacy of the slant depth design to enhance the bearing performance. The results have also revealed the possibility of realizing a significant reduction in development and testing time with the promising application of CFD tools in the design of HGJBs.

NOMENCLATURE

c radial clearance;
C eccentricity;
D bearing diameter;
e Fourier number;
F_{cond} condensation coefficient;
F_{evap} evaporation coefficient;
F_T oil film tangential force;
F_R oil film radial force;
$\overline{F_R}$ dimensionless radial stiffness $\overline{F_R} = \dfrac{2\pi \overline{W} \cos\phi}{\varepsilon}$;
I unit tensor;
L bearing length;
p local far-field pressure;
p_b bubble surface pressure;
P static pressure;
$\overline{P}$ dimensionless pressure $\overline{P} = \dfrac{P}{\mu\omega}\left(\dfrac{c}{R}\right)^2$;
R bearing radius;
R_b bubble radius;
R_c, R_e mass transfer source terms connected to the growth and collapse of the vapor bubbles, respectively;
R_j journal radius;
t time;
T bearing friction torque;
$\overline{T}$ dimensionless friction torque $\overline{T} = \dfrac{T}{\mu\omega R^3}\left(\dfrac{c}{R}\right)$;
w bearing width;
W bearing load capacity;
$\overline{W}$ dimensionless load capacity $\overline{W} = \dfrac{W}{\mu\omega R^2}\left(\dfrac{c}{R}\right)^2$;
α groove angle;
ε eccentricity ratio;
θ angular coordinate;
μ fluid viscosity;
μ_v vapor viscosity;
ρ fluid density;
ρ_l liquid density;
ρ_v vapor density;
σ liquid surface tension coefficient;
τ_{yx} stress tensor;
ϕ attitude angle;
ω rotational speed of journal;

REFERENCES

1. Venkatesh, V. C., *Precision Engineering*, Tata McGraw-Hill Education, New Delhi (2007).
2. Feng, M. and Kenjo, T., "Friction and Wear of Spindle Motor Hydrodynamic Bearings for Information Storage Systems during Startup and Shutdown," *Microsystem Technologies*, **13**, pp. 987-997 (2007).
3. Tribology Series, Hydrodynamic Lubrication, *Tribology and Interface Engineering Series*, **24**, pp. 121-240 (1993).
4. Gad, A. M., Nemat-Alla, M. M., Khalil, A. A. and Nasr, A. M., "On the Optimum Groove Geometry for Herringbone Grooved Journal Bearings," *Journal of Tribology*, **128**, pp. 585-593 (2006).
5. Zhang, X. *et al*., "Load Carrying Capacity of Misaligned Hydrodynamic Water-Lubricated Plain Journal Bearings with Rigid Bush Materials," *Tribology International*, **99**, pp. 1-13 (2016).

https://doi.org/10.1017/jmech.2017.72 Published online by Cambridge University Press

6. Hirs, G. G., "The Load Capacity and Stability Characteristics of Hydrodynamic Grooved Journal Bearings," *ASLE Transactions*, **8**, pp. 296-305 (1965).
7. Besanjideh, M. and Gandjalikhan Nassab, S. A., "Effect of Lubricant Compressibility on Hydrodynamic Behavior of Finite Length Journal Bearings Running under Heavy Load Conditions," *Journal of Mechanics,* **32**, pp. 101-111 (2016).
8. Scheichl, B., Neacsu, I. A. and Kluwick, A., "A Novel View on Lubricant Flow Undergoing Cavitation in Sintered Journal Bearings," *Tribology International*, **88**, pp. 189-208 (2015).
9. Kinouchi, K. and Tanaka, K., "Performance Characteristics of Herringbone-Grooved Journal Bearings Using a Finite Element Method," *Proceedings of the Japan International Tribology Conference*, pp. 935-940 (1990).
10. Adatepe H., Bykloglu A. and Sofuoglu, H., "An Investigation of Tribological Behaviors of Dynamically Loaded Non-Grooved and Micro-Grooved Journal Bearings," *Tribology International*, **58**, pp. 12-19 (2013).
11. Lee, W. S., Ma, R. H., Wu, W. F., Chen, S. L. and Hsia, H. W., "Performance and Bearing Load Analysis of a Twin Screw Air Compressor," *Journal of Mechanics*, **15**, pp. 69-78 (1999).
12. Chen, C. Y., Liu, C. S., Tee, C. K. and Li, Y. C., "Application of Stabilized Term in Free Boundary Problems for Optimizing Bi-Directional-Rotation Herringbone-Grooved Journal Bearings," *Applied Mathematics* (2016).
13. Chang, B. H., Chen, P. H. and Lee, D. S., "Experimental Stability Study on Herringbone-Microgrooved Journal Bearing in an Impeller-Spindle," *Journal of Mechanics*, **28**, pp. 123-133 (2012).
14. Jang, G. H. and Chang, D. I., "Analysis of Hydrodynamic Herringbone Grooved Journal Bearing Considering Cavitation," *Journal of Tribology*, **122**, pp. 103-109 (2000).
15. Jang, G. H. and Yoon, J. W., "Nonlinear Dynamic Analysis of a Hydrodynamic Journal Bearing Considering the Effect of Rotating or Stationary Groove," *Journal of Tribology*, **124**, pp. 297-304 (2002).
16. Jang, G. H. and Yoon, J. W., "Stability Analysis of a Hydrodynamic Journal Bearing with Rotating Herringbone Grooves," *Journal of Tribology*, **125**, pp. 291-300 (2003).
17. Narendiranath Babu, T., Manvel Raj, T. and Lakshmanan, T., "A Review on Application of Dynamic Parameters of Journal Bearing for Vibration and Condition Monitoring," *Journal of Mechanics*, **31**, pp. 391-416 (2015).
18. Yen, R. H. and Chen, C. Y., "Enhancement of Journal Bearings Characteristics Using Novel Elliptical Grooves," *Proceedings of the Institution of Mechanical Engineers, Part J: Journal of Engineering Tribology*, **224**, pp. 259-269 (2010).
19. Chen, S. K., Chou, H. C. and Kang, Y., "Stability Analysis of Hydrodynamic Bearing with Herringbone Grooved Sleeve," *Tribology International*, **55**, pp. 15-28 (2012).
20. *ANSYS FLUENT, Version 15.0: User Manual*, ANSYS, Inc.: Canonsburg, USA (2013).
21. Lee, T. S., Liu, Y. G. and Winoto, S. H., "Analysis of Liquid-Lubricated Herringbone Grooved Journal Bearings," *International Journal of Numerical Methods for Heat & Fluid Flow*, **14**, pp. 341-365 (2004).
22. Zwart, P. J., Gerber, A. G. and Belamri, T., "A Two-Phase Flow Model for Predicting Cavitation Dynamics," *Proceedings of the Fifth International Conference on Multiphase Flow*, Yokohama, Japan (2004).
23. Gao, G., Yin, Z., Jiang, D. and Zhang, X., "Numerical Analysis of Plain Journal Bearing under Hydrodynamic Lubrication by Water," *Tribology International*, **75**, pp. 31-38 (2014).
24. Gertzos, K. P., Nikolakopoulos, P. G. and Papadopoulos, C. A., "CFD Analysis of Journal Bearing Hydrodynamic Lubrication by Bingham Lubricant," *Tribology International*, **41**, pp. 1190-1204 (2008).
25. Viswanath, D. S., Ghosh, T., Prasad Dasika, H. L., Dutt Nidamarty, V. K. and Rani, K. Y., *Viscosity of Liquids: Theory, Estimation, Experiment, and Data*, Softcover Reprint of Hardcover 1st ed. 2007 Edition, Springer Netherlands, Dordrecht (2009).
26. *Mystik® Power Lubricants® Premium Fleet Motor Oil. SAE 30 Material Safety Data Sheet*, CITGO Petroleum Corporation (2009).
27. Van Doormaal, J. P. and Raithby, G. D., "Enhancements of the SIMPLE Method for Predicting Incompressible Fluid Flows," *Numerical Heat Transfer*, **7**, pp. 147-163 (1984).
28. Jang, D. S., Jetli, R. and Acharya, S., "Comparison of the PISO, SIMPLER, and SIMPLEC Algorithms for the Treatment of the Pressure–Velocity Coupling in Steady Flow Problems," *Numerical Heat Transfer*, **10**, pp. 209-228 (1986).
29. Jakobsson, B. and Floberg, L., "The Finite Journal Bearing Considering Vaporization," *Transactions of Chalmers University of Technology,* Guthenburg, Sweden, **190** (1957).
30. Chao, P. C. P. and Huang, J. S., "Calculating Rotordynamic Coefficients of a Ferrofluid-Lubricated and Herringbone-Grooved Journal Bearing via Finite Difference Analysis," *Tribology Letters*, **19**, pp. 101-110 (2005).
31. Chen, C. Y., Liu, C. S. and Li, Y. C., "Shannchyi Mou. Geometry Optimization for Asymmetrical Herringbone Grooves of Miniature Hydrodynamic Journal Bearings by Using Taguchi Technique," *Proceedings of the Institution of Mechanical Engineers, Part J: Journal of Engineering Tribology*, **229**, pp. 196-206 (2015).

https://doi.org/10.1017/jmech.2017.72 Published online by Cambridge University Press

32. Kawabata, N., Ozawa, Y., Kamaya, S. and Miyake, Y., "Static Characteristics of the Regular and Reversible Rotation Type Herringbone Grooved Journal Bearing," *Journal of Tribology*, **111**, pp. 484-490 (1989).

(Manuscript received March 3, 2017,
accepted for publication June 19, 2017.)

https://doi.org/10.1017/jmech.2017.72 Published online by Cambridge University Press